

Coseismic Deformation from the 1999 M_w 7.1 Hector Mine, California, Earthquake as Inferred from InSAR and GPS Observations

by Mark Simons, Yuri Fialko,* and Luis Rivera

Abstract We use interferometric synthetic aperture radar (InSAR) and Global Positioning System (GPS) observations to investigate static deformation due to the 1999 M_w 7.1 Hector Mine earthquake, that occurred in the eastern California shear zone. Interferometric decorrelation, phase, and azimuth offset measurements indicate regions of surface and near-surface slip, which we use to constrain the geometry of surface rupture. The inferred geometry is spatially complex, with multiple strands. The southern third of the rupture zone consists of three subparallel segments extending about 20 km in length in a N45°W direction. The central segment is the simplest, with a single strand crossing the Bullion Mountains and a strike of N10°W. The northern third of the rupture zone is characterized by multiple splays, with directions subparallel to strikes in the southern and central. The average strike for the entire rupture is about N30°W. The interferograms indicate significant along-strike variations in strain which are consistent with variations in the ground-based slip measurements. Using a variable resolution data sampling routine to reduce the computational burden, we invert the InSAR and GPS data for the fault geometry and distribution of slip. We compare results from assuming an elastic half-space and a layered elastic space. Results from these two elastic models are similar, although the layered-space model predicts more slip at depth than does the half-space model. The layered model predicts a maximum coseismic slip of more than 5 m at a depth of 3 to 6 km. Contrary to preliminary reports, the northern part of the Hector Mine rupture accommodates the maximum slip. Our model predictions for the surface fault offset and total seismic moment agree with both field mapping results and recent seismic models. The inferred shallow slip deficit is enigmatic and may suggest that distributed inelastic yielding occurred in the uppermost few kilometers of the crust during or soon after the earthquake.

Introduction

Recent advances in remote sensing, in particular interferometric synthetic aperture radar (InSAR) and construction of dense Global Positioning System (GPS) networks permit us to form high-resolution maps of earthquake-induced surface deformation at a centimeter-scale accuracy. We report on observations of surface displacements due to the 16 October 1999 M_w 7.1 Hector Mine earthquake in California. This earthquake occurred in the Mojave Desert, rupturing the northwest-trending Bullion and Lavic Lake faults, which are part of the eastern California shear zone (ECSZ) (Scientists of the USGS *et al.*, 2000; Treiman *et al.*, 2002). The tectonically active ECSZ is believed to accommodate about 15% of the relative motion between the North American and

Pacific plates, with an estimated strain accumulation rate of the order of 1 cm/yr across the ~80-km-wide shear zone (e.g., Sauber *et al.*, 1986; Dokka and Travis, 1990).

The M_w 7.3 Landers earthquake (e.g., Sieh *et al.*, 1993) occurred 7 years before and about 20 km to the west of the Hector Mine earthquake. Such a close temporal and spatial proximity has raised the question of a possible causal relationship between these earthquakes (Parsons and Dreger, 2000; Scientists of the USGS *et al.*, 2000; Freed and Lin, 2001). Both the Landers and Hector Mine earthquakes initiated robust aftershock sequences, as well as triggering seismicity as far as several hundred kilometers from the rupture plane (Hauksson *et al.*, 2002). Before addressing the relationship between these two earthquakes and the nature of postseismic deformation from the Hector Mine event (e.g., Pollitz *et al.*, 2001; Hudnut *et al.*, 2002; Pollitz and Sacks, 2002; Masterlark and Wang, 2002; Owen *et al.*, 2002), we

*Present address: Institute of Geophysics and Planetary Physics, University of California–San Diego, La Jolla, California.

must first construct the most reliable coseismic slip model possible. Of particular relevance to postseismic models is the depth extent of slip in relation to the depth at which we expect viscous creep to begin. Here, we construct a slip model using available InSAR and GPS data. These models require both reasonable constraints on the fault geometry and an assumed rigidity structure. We use the InSAR observations to constrain the fault geometry and explore the effect of assuming different layered elastic structures.

Observations of Surface Deformation and Fault Rupture

The epicentral area of the Hector Mine earthquake has been imaged by the ERS-1 and ERS-2 C-band radar satellites since 1992. Location of the earthquake rupture from field mapping (Treiman *et al.*, 2002) and the radar scenes used in this study are shown in Figure 1. InSAR data that cover the date of the earthquake consist of several interferometric pairs from both the descending and ascending satellite orbits with B_{\perp} less than 200 m (B_{\perp} is the perpendicular component of the interferometric baseline). The interferometric data that most tightly bracket the earthquake date are a 35-day pair from a descending (DSC) orbit, hereafter referred to as IP1, and an approximately 4-year ascending (ASC) pair, hereafter referred to as IP2 (Table 1). Independent preseismic interferograms from both orbits (e.g., ASC: 20 May 1995 to 8 August 1999; DSC: 22 July 1998 to 15 September 1999, not shown here) show no significant deformation in the study area prior to the earthquake. Therefore, the long-term interferograms that span the earthquake date are likely to be dominated by the coseismic signal. In addition to the radar data, we use the GPS data from 35 continuous Southern California Integrated GPS Network (SCIGN) stations located within 150 km from the epicenter (Scientists of the USGS *et al.*, 2000; Hurst *et al.*, 2000) and 76 campaign-mode measurements in the near field of the earthquake (Agnew *et al.*, 2002) (Fig. 1).

The interferometric data are processed using the Caltech/JPL radar processing software ROI_PAC. To remove effects of topography, we use a mosaic of 224 U.S. Geological Survey (USGS) digital elevation models (DEMs) with 30-m postings. IP1 and IP2 have small B_{\perp} values (about 20 and 50 m, respectively), suggesting that their sensitivity to errors in the DEM is relatively small. After corrections for topography, we filter, unwrap, and map the interferograms from the original SAR coordinate system onto a geographic grid.

We first consider the interferometric coherence from IP1. We focus on IP1 because it has the shortest time span (35 days) and therefore has experienced minimum decorrelation (Zebker and Villasenor, 1992). Figure 2 shows the coherence map for IP1. We calculate the coherence in 5-by-5-pixel windows using the detrended scatter in the interferometric phase (Goldstein and Werner, 1998). Decorrelation is caused by changes in the reflective properties of the ground (Zebker and Villasenor, 1992). Because the radar coherence away from the fault is uniformly high, the near-

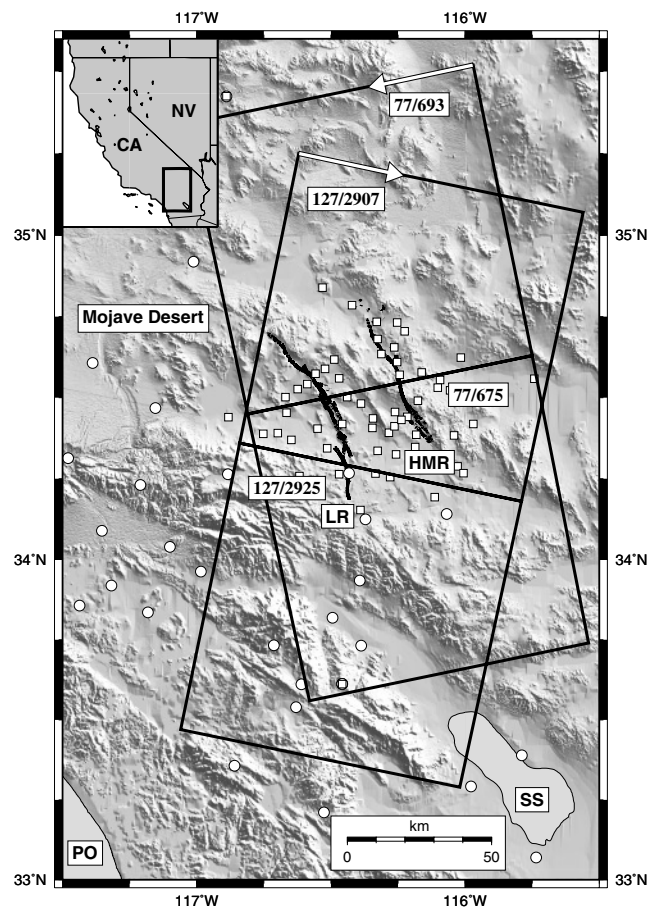


Figure 1. Shaded relief map of the area of study, with the area indicated by the outlined box in the index map at the top left. Surface rupture of the Landers (LR) and Hector Mine (HMR) earthquakes shown by a heavy black lines (Treiman *et al.*, 2002). Solid squares denote ERS radar scenes for the ascending (track 77, frames 675 and 693), and descending (track 127, frames 2907 and 2925) orbits. White arrows indicate the satellite look direction (ground to satellite). Circles and squares show positions of continuous and campaign-style GPS benchmarks, respectively. The Salton Sea and the Pacific Ocean are indicated by SS and PO, respectively.

fault decorrelation likely results from earthquake effects. In particular, we attribute linear zones of decorrelation seen in Figure 2 to surface faulting or disturbed ground caused by intense shaking. The decorrelation lineaments may reflect either true changes in the ground reflectivity (e.g., due to intense deformation) or gradients in the line-of-sight displacements in excess of the resolution limit $\lambda/2\Delta R$, where λ is the radar wavelength (~ 5.7 cm), and ΔR is the pixel size in range (~ 20 m). We note that averaging over the 5-by-5-pixel window used in our analysis of the radar phase correlation implies a lower bound on the width of the imaged decorrelation zones of the order of 100 m. The coherence data alone provide a unique approach to mapping surface rupture and detecting earthquake-induced damage. In order

Table 1
Interferometric Pairs Considered

Direction	Interferometric Pair	mean RMS (cm)	B_{\perp} (m)
DSC	1999/11/24–1997/01/08 (IP3)	2.24	99
DSC	2000/07/26–1997/03/19	2.71	59
DSC	2000/03/08–1997/01/08	2.78	119
DSC	2000/07/26–1997/07/02	2.87	92
DSC	1999/12/29–1995/12/19	2.90	28
DSC	1999/10/20–1999/09/15 (IP1)	3.01	23
DSC	2000/07/26–1999/09/15	3.24	203
DSC	1999/10/20–1998/07/22	3.42	44
DSC ¹	2000/04/12–1995/12/20	3.44	87
DSC	2000/08/30–1995/10/10	3.57	46
DSC	2000/08/30–1999/06/02	11.45	143
ASC	1999/11/21–1995/11/12 (IP2)	—	49

DSC indicates a descending orbit (frames 2907 and 2925); ASC, an ascending orbit (frames 675 and 693). B_{\perp} corresponds to the perpendicular component of the baseline.

¹Only frame 2907.

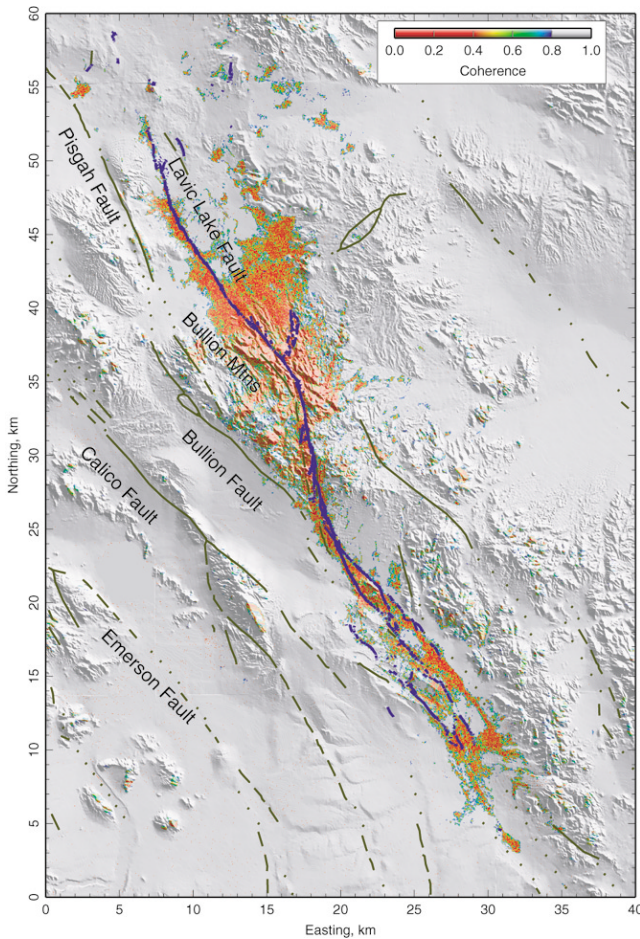


Figure 2. Interferometric coherence, C , for IP1, with $C > 0.8$ set to be transparent. Brown lines indicate known faults (Jennings, 1994). Surface rupture as observed in the field is indicated by the blue line (Treiman *et al.*, 2002). UTM zone 11 projection with origin at (116.457W 34.250N).

to minimize non-earthquake-related decorrelation and maximize the utility of coherence in the future, it is important to use the shortest time interval possible spanning the earthquake.

Figure 3 shows the interferometric fringes in the earthquake rupture area from IP1. Each fringe represents 2.8 cm of motion in the satellite line-of-sight (LOS) direction. In many places along the southern portion of the fault, fringes extend continuously to within about 100 m from the surface rupture. The scalloped fringe patterns seen along strike reveal complex deformation within the fault zone. Such complexity is also documented by field work (Treiman *et al.*, 2002). The corresponding fringe pattern from the ascending interferogram (IP2) is shown in Figure 4. IP2 has more extensive regions of decorrelation due to the 4-year time interval spanned by the interferogram. This temporal decorrelation is most prevalent in areas with sand dunes or steep terrain and does not necessarily indicate continued fault slip, but most likely erosion, wind action, and disruption due to human activity.

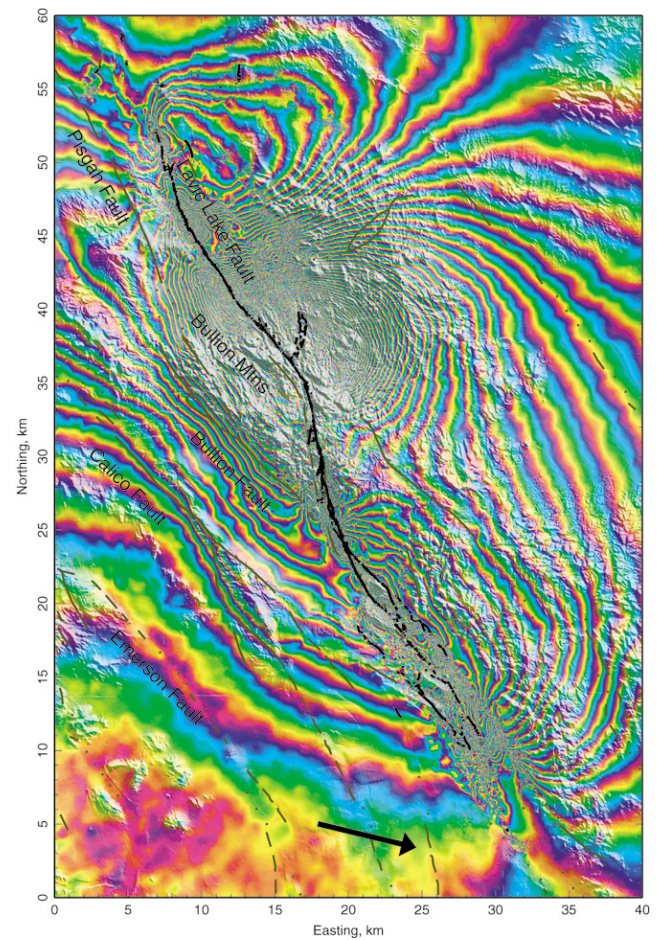


Figure 3. Same as Fig. 2 but color indicates wrapped phase for IP1. Each color cycle represents 2.8 cm of motion in the line-of-sight (LOS) direction. The black arrow represents the horizontal projection of the LOS vector toward the satellite.

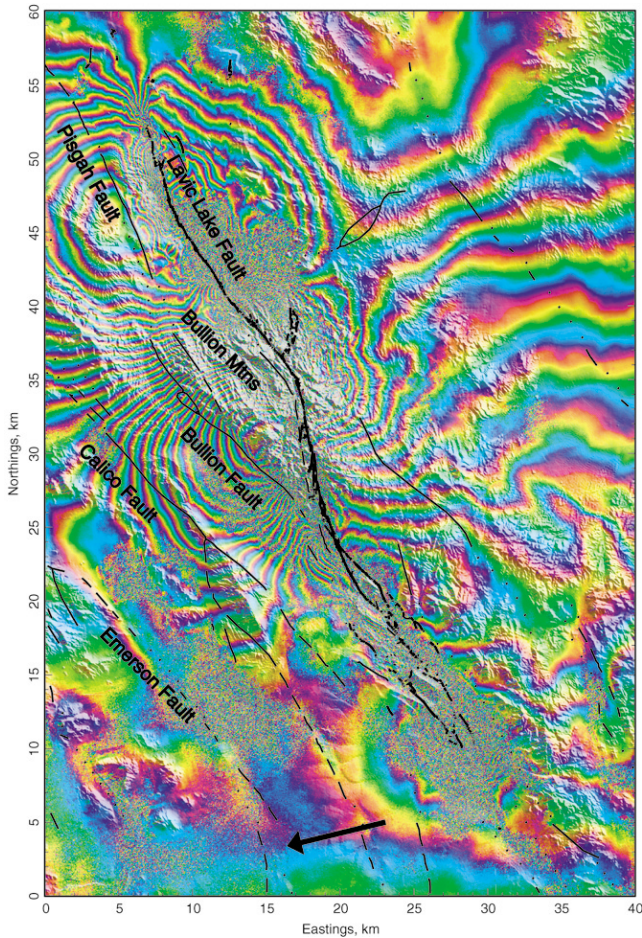


Figure 4. Same as Fig. 3, but color indicates wrapped phase for IP2.

In addition to the satellite LOS measurements employing the radar phase, we calculate azimuth offsets (AZO) of the radar images by spatial cross-correlation of pixels using the radar amplitude (Fig. 5). These offsets provide measurements of the horizontal displacements in the direction of the satellite heading. At full resolution, the pixel size of a radar scene is about 4 m in the azimuth (along-track) directions. While it is also possible to calculate the range offsets, the latter are redundant with the phase measurements, but are far less accurate. For this reason, we do not use range offsets in our analyses. We estimate typical AZO errors are on the order of 10 to 20 cm. While the AZO data are less precise than the LOS (phase) data, they are useful in that they measure the horizontal component of deformation in a projection that is orthogonal to the satellite LOS direction. Because of vanishing signal-to-noise ratio beyond about 40 km from the epicenter, we analyze the AZO data for only a subarea of the descending interferogram IP1 encompassing the earthquake rupture. AZO data from the interferometric pairs having larger time spans are considerably noisier. One can convert the three independent radar measurements of the coseismic deformation (e.g., IP1-phase, IP1-AZO, and IP2-phase) to

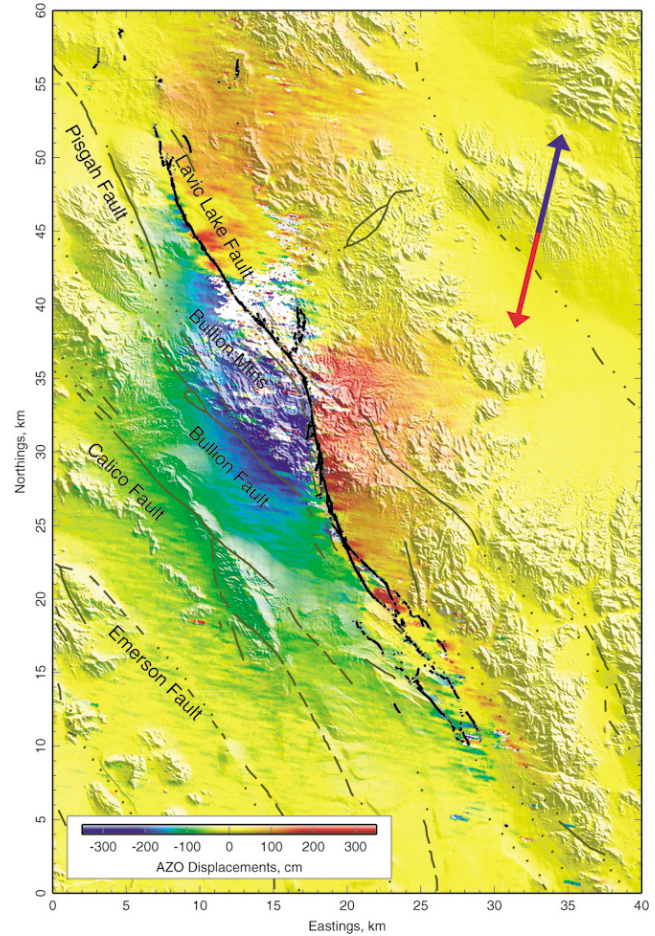


Figure 5. Same as Fig. 3, but color indicates AZO observations. Arrows represents the horizontal component of motion indicated by the respective colors.

conventional (East, North, Up) displacement vector fields (e.g., Fialko *et al.*, 2001); however, for the purposes of modeling the coseismic deformation, we use only the original InSAR-GPS measurements.

We infer the earthquake rupture geometry using the interferometric images and relocated postearthquake seismicity (Hauksson *et al.*, 2002) (Fig. 6). We identify several primary fault segments, as illustrated in Figure 6. The southern section of the fault consists of three subparallel strands delineated by regions of low phase coherence (Fig. 2). The central and western strands (subfaults 1 and 2 in Fig. 6) coincide with the geologically mapped surface rupture. Interestingly, the easternmost strand (subfault 3) stands out as the most prominent decorrelation lineament (Fig. 2) but was not identified during the postearthquake field survey of the rupture area. A later field investigation, using the coherence map from IP1 as a guide, discovered about 60 cm of right-lateral offset on this previously unreported surface rupture (Treiman *et al.*, 2002). The central portion of the surface rupture is characterized by a localized linear zone of low coherence as the rupture crosses into the Bullion Mountains

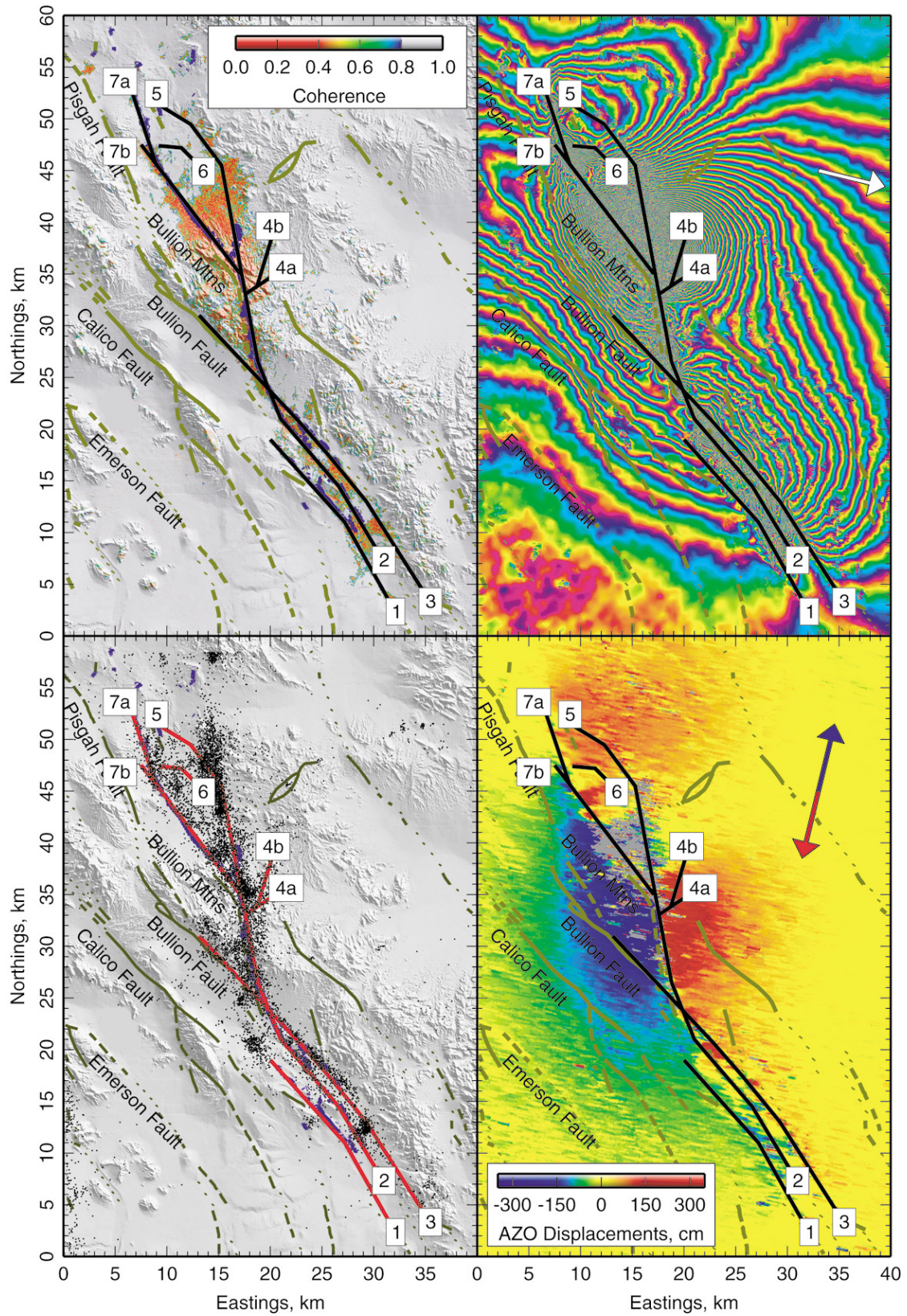


Figure 6. Primary inferred fault segments. Segments are shown with coherence from IPI (top left), the IPI interferogram (top right), relocated seismicity for all of 2000 (Hauksson *et al.*, 2002) (bottom left), and the azimuth offsets from IPI (bottom right).

(Fig. 6). In this region, the AZO measurements indicate about 5 to 6 m of horizontal relative motion. The decorrelation zone widens considerably to the north, following the mapped surface break, as well as extending through Lavic Lake playa. The widening of the decorrelation zone to the north-east of the epicenter may be due to intense surface disruption between the subparallel fault strands revealed by the post-earthquake seismicity (Fig. 6).

Inversion of InSAR and GPS Data for Subsurface Slip Distribution

The unwrapped interferometric phase carries information about relative displacements of the Earth's surface in the radar LOS direction. The phase may also be affected by propagation effects (in particular, atmospheric delays) and imprecise knowledge of the satellite orbits. By using multiple independent interferometric pairs that include the earthquake date, it is possible to estimate the measurement errors in the radar LOS displacements and to select the data that are least affected by the time-dependent atmospheric noise. In particular, an interferometric pair that is quantitatively most similar to other independent interferograms is likely to have the least atmospheric contamination. We analyzed 11 coseismic interferograms from the descending orbit that span time intervals from about 1 month to 4 years (Table 1). We evaluate the similarity of interferograms by calculating the root mean square (rms) difference between a particular interferogram and all the remaining pairs. To account for a small yet detectable postseismic deformation (Jacobs *et al.*, 2002), we subtract the postseismic interferometric pair 2000/07/26–1999/10/20 from all interferometric pairs shown in Table 1 except the short-term IP1. Before we calculate the rms difference, the phase difference is detrended by subtracting a planar ramp that best fits the entire radar scene. Such detrending minimizes a possible bias due to uncertainties in the satellite orbits. The remaining misfit is likely dominated by time-dependent atmospheric noise.

The mean rms misfit characterizes the degree of overall similarity between a given interferogram and all other interferograms in the set. As apparent from Table 1, the DEM errors are negligible, because interferograms with smallest perpendicular baselines B_{\perp} (i.e., the ones that are least sensitive to topography) do not exhibit the smallest rms misfits. All interferometric pairs seem to contain atmospheric fluctuations of the order of 1 cm, except the 2000/08/30–1999/06/02 pair, which seems to be severely affected by atmospheric noise. IP1 also does not have the least amount of atmospheric noise (as confirmed by our inversions and analysis of preseismic pairs that include the 1999/09/15 scene). Therefore, for modeling of the coseismic deformation, we use the descending interferometric pair 1999/11/24–1997/01/08, hereafter referred as IP3, as it seems to be the least affected by the atmospheric noise (Table 1) and has a time span that is similar to that of the ascending pair IP2. Because

slave images in both IP2 and IP3 were acquired in late November, 1999, they include some postseismic deformation that has occurred within 1 month after the earthquake. Analysis of postseismic InSAR and continuous GPS data indicates that the corresponding postseismic deformation constitutes a negligible fraction of the coseismic signal (Jacobs *et al.*, 2002).

We detrend the unwrapped interferograms to correct for possible uncertainties in satellite orbits. In the presence of deformation having a characteristic wavelength on the order of, or exceeding the radar scene size, as is the case for the Hector Mine earthquake, removal of a best-fitting ramp may affect the long-wavelength part of the tectonic signal. Sandwell *et al.* (2000) argue that the available orbits may be precise enough so that no flattening is required. We reduce the effects of orbit errors by solving for the best-fitting bilinear ramps in the data as a part of the inversion and using GPS measurements as ground truth. We find that even the flattened LOS displacement images may contain long-wavelength ramps on the order of several centimeters across a radar scene. Systematic along-scene variations in the InSAR–GPS misfit on the order of several tens of centimeters are obtained for the AZO data. These results suggest that for the existing ERS-1 and ERS-2 data, *a priori* information about the earthquake-induced deformation from modeling or GPS measurements may be necessary for better estimates of orbital errors. After adjustment of the long-wavelength ramps, the available GPS data agree with the InSAR-derived displacements (Fialko *et al.*, 2001).

To account for the complex geometry of the Hector Mine rupture, we approximate the fault geometry by five rectangular fault segments. The length (along-strike dimension) and strike of the segments is determined based on the InSAR and field mapping data. The width (down-dip dimension) of the fault segments is assumed to be 20 km. To allow for a spatially heterogeneous slip on the fault, we subdivide the rectangular segments into smaller slip patches. The patch size increases with depth to maintain a more uniform resolution of slip, essentially making the model resolution matrix more diagonal. The actual progression of patch size with depth is determined empirically, using the actual data. The shallowest patches are approximately 900 m by 800 m (Figs. 7 and 8).

Inversion of the InSAR data at full resolution (geocoded pixel size of 30 m) requires evaluation of a forward model at more than 10^7 points, which is an impractical task. After averaging the InSAR data over 8- by 8-pixel bins (pixel size of 240 m), the data set contains on the order of 10^5 data points. More averaging may be performed to decrease the number of observation points still, but at the expense of a loss in resolution in the near field. We point out that even in the absence of computational constraints, the use of an entire InSAR dataset is not warranted because the far-field deformation can be adequately described by a relatively small number of data points. Also, the LOS and AZO offset measurements are not uncorrelated from pixel to pixel (Emard-

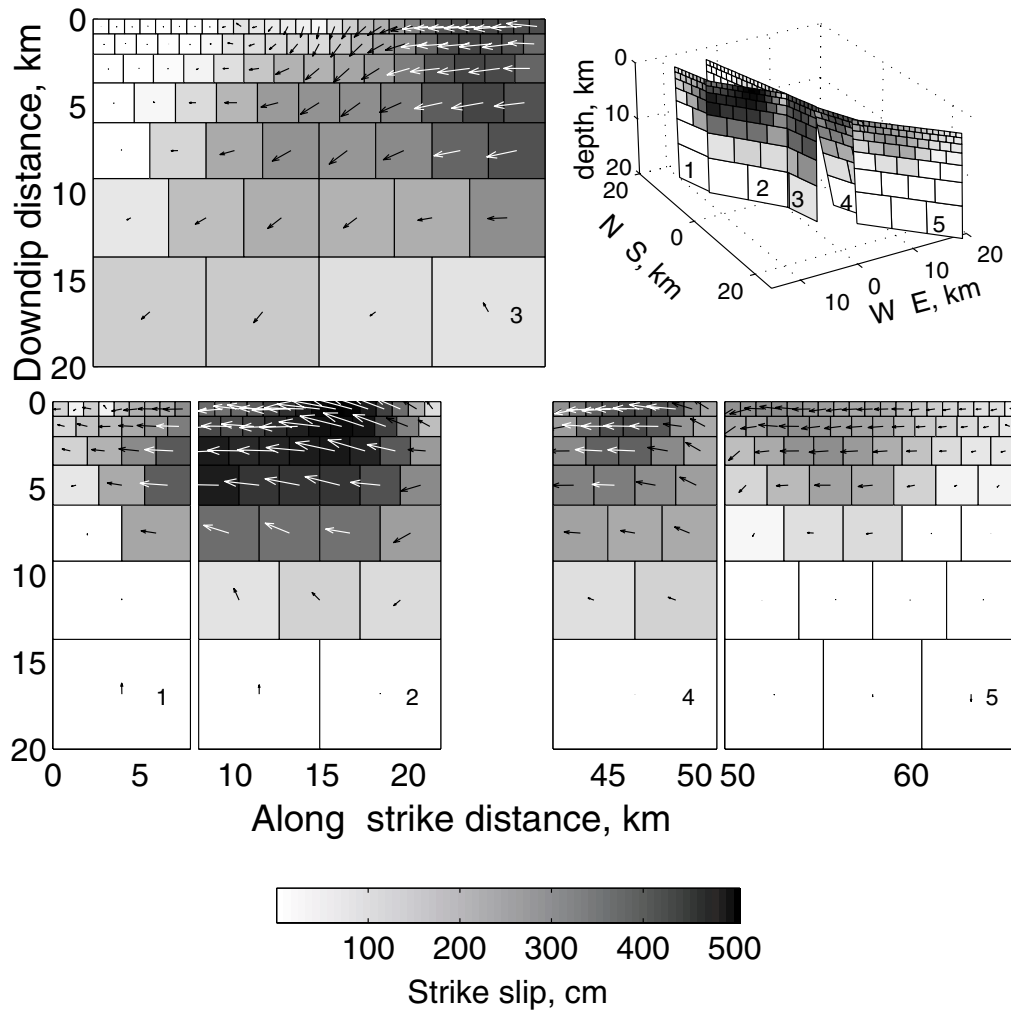


Figure 7. Slip distribution from the joint inversion of the InSAR–GPS data using an elastic half-space model. Shading intensity denotes the amplitude of the strike-slip displacements, and arrows show the direction of slip on the western side of the Hector Mine rupture, viewing from west to east.

son *et al.*, 2002). To reduce the computational task, we subsample the InSAR data according to an algorithm whereby the sampling density is proportional to the curvature (second spatial derivative) of the displacement field. A maximum spacing of ~10 km is used to sample the far-field data (farther than 40 km from the epicenter), and the sampling algorithm controls finer sampling (Fig. 9a,b). The number of selected data points is two orders of magnitude less than the number of data points in the original data set. This sampling approach has the effect of making the data resolution matrix more diagonal.

The use of variable sampling of the InSAR data, as well a combination of different datasets (e.g., LOS, AZO, and continuous GPS data), in a joint inversion necessitates some choice of weighting of the data. The InSAR data points are weighted in proportion to the area represented in the original image by a selected subset of pixels,

$$w_i = \frac{Nn_i^{1/2}}{\sum_{j=1}^N n_j^{1/2}}, \tag{1}$$

where w_i is the weight of a data point i in a subsampled selection, n_i is the number of points in the original interferogram represented by a point i , and N is the total number of points in the interferogram. The GPS data are assigned weights by

$$w_i = \frac{M}{\sigma_i \sum_{j=1}^M \sigma_j^{-1}}, \tag{2}$$

where τ_i and σ_j represent 1 = sigma errors for a particular component of a displacement vector at a given benchmark, and M is a total number of measurements (i.e., a total number of the GPS benchmarks times three). After normalization,

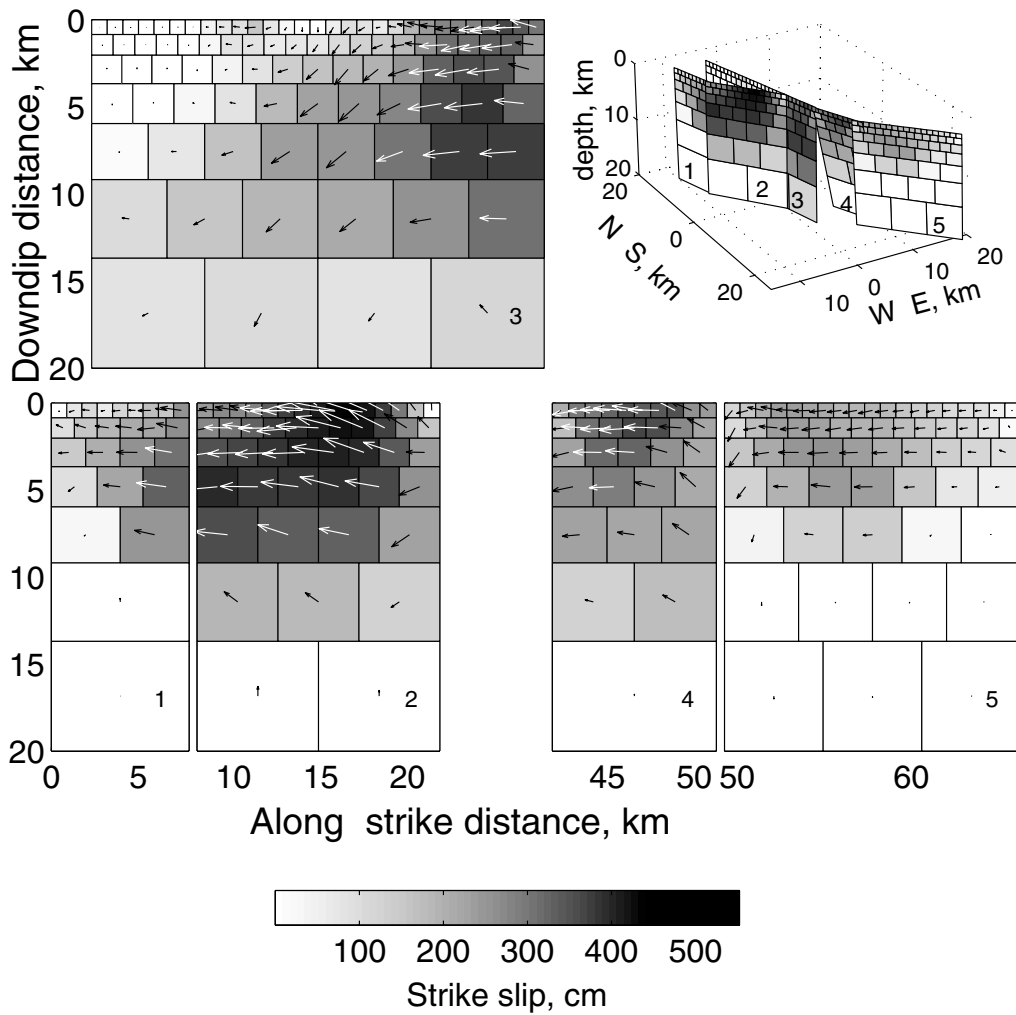


Figure 8. Same as Figure 7, but using a layered elastic space model.

the sum of weights for each dataset equals unity, $\sum w_i = 1$. The relative weighing of different datasets in our inversion is achieved by dividing the normalized weights w_i by a scaling factors α_k , where index $k = l, a$, and g , which correspond respectively to the LOS, AZO, and GPS datasets, to form the data covariance matrixes $C^j = \alpha_k^{-1} w_i$. Factors α_k represent relative errors of each data set; we find (based on many simulations) that values $\alpha_l = 1$, $\alpha_a = 20$, and $\alpha_g = 0.2$ (units of displacement) allow us to fit each single dataset without substantially degrading the quality of fit to other data.

We wish to find a distribution of slip, $\mathbf{u} = (u_s, u_d)$, where u_s and u_d are the strike-slip and dip-slip components of slip on a fault, respectively, that yields a minimum L_2 norm solution to a system of equations

$$\begin{aligned}
 C^l(G_l \mathbf{u} + R_l) &= C^l \mathbf{d}_l \\
 C^a(G_a \mathbf{u} + R_a) &= C^a \mathbf{d}_a \\
 C^g G_g \mathbf{u} &= C^g \mathbf{d}_g \\
 \lambda^{-1} \nabla \mathbf{u} &= 0
 \end{aligned} \tag{3}$$

where G_j are the synthetic Green's functions, R_l and R_a are the bilinear ramps representing possible errors in the LOS and AZO data due to errors in the orbital information, and \mathbf{d}_j are the data vectors. The last equation in system (3) is a smoothing operator that minimizes the slip gradient, λ^{-1} being the effective damping coefficient. The smoothing is implemented using finite-difference quadrature for the first spatial derivative of slip. To further regularize the problem, we require that the strike-slip motion on the faults cannot be left-lateral; no constraints are imposed on the dip-slip component. Equations (3) constitute an overdetermined linear system of equations that can be inverted for the slip distribution \mathbf{u} and InSAR ramp coefficients R , provided Green's functions G_j are known. We fix the width and length of the fault subsegments and require that the top edges of the segments reside at the free surface, but the strike, dip, and horizontal position of the segments are allowed to vary. Because the fault geometry is not specified *a priori*, the problem is nonlinear and has to be solved iteratively. In our starting model, the positions of the top edges of the subfaults are

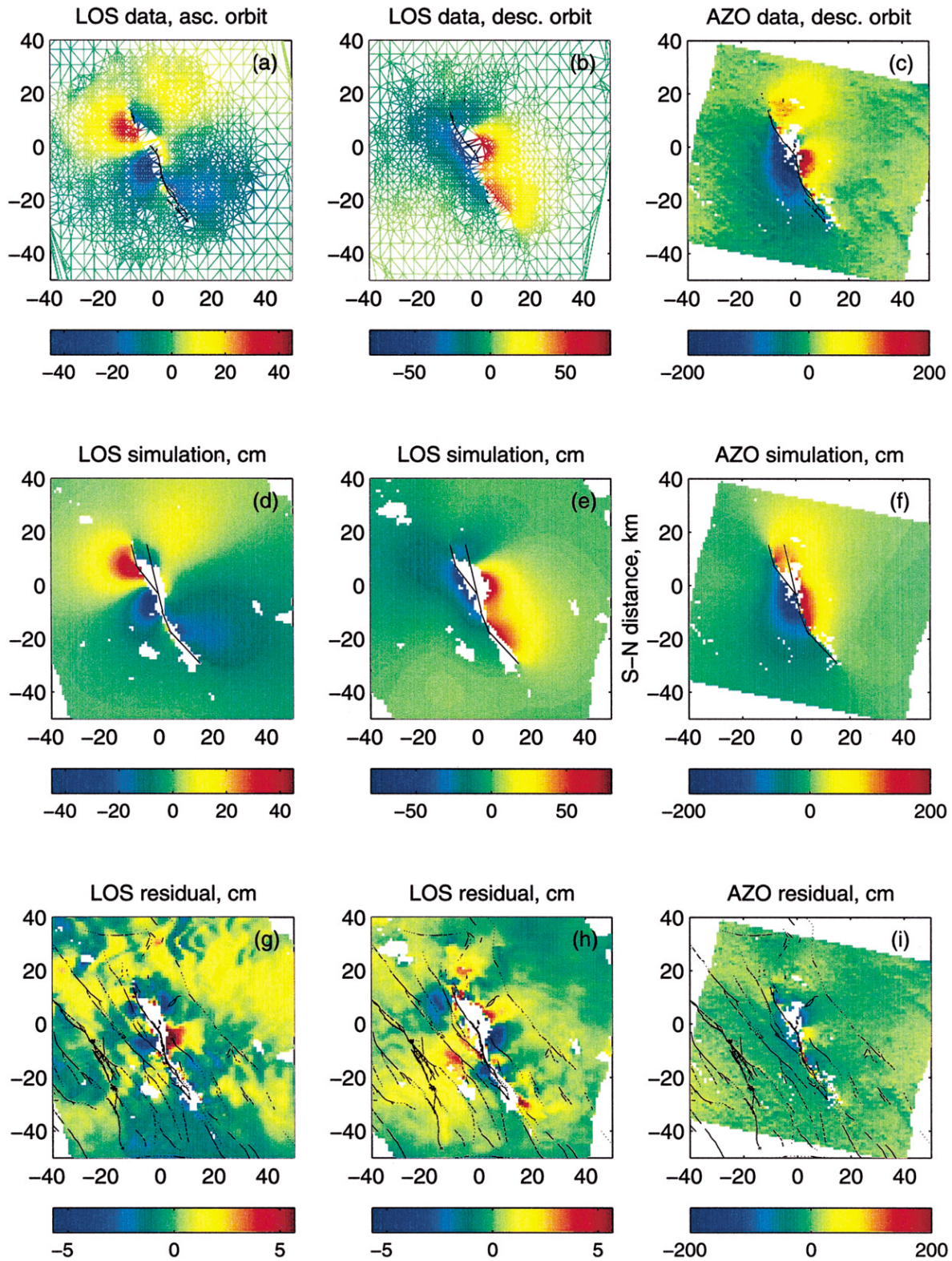


Figure 9. (a) and (b) Subsampled LOS phase data used in the inversion (parts of interferograms beyond the region shown are sampled at a base spacing of ~ 10 km). (c) AZO data. (d)–(f) Best-fitting models. (g)–(i) Residuals after subtracting the models predictions from the data. Note the change in color scale for (g) and (h). In (a)–(i), the origin corresponds to the earthquake epicenter (116.27°W , 34.595°N).

prescribed based on the InSAR, field mapping, and after-shock data. The initial fault dips are assumed to be vertical. We perform a 20-parameter (i.e., four geometric parameters consisting of two spatial coordinates and the fault strike and dip angles for each of five subfaults) forward grid search for an optimal subfault orientation. At each step we recalculate the appropriate Green's functions G_j , invert the system (3), and evaluate the least square residual between the model and the data. We accept changes in the fault geometry if they produce more than 1% reduction in the rms misfit between the model and the data.

Typically, inversions of geodetic data for fault slip have relied on elastic half-space models. Here, we compare predictions of a homogeneous elastic half-space model with those of a horizontally layered elastic model. We use the rigidity structure inferred from the seismic velocity structure proposed by Jones and Helmberger (1998), which is derived to explain seismic waveform data in the eastern California shear zone. The corresponding rigidity model consists of three layers overlying a half-space (Fig. 10). The rigidity gradients in the top 6 km of this model are potentially important, given that slip produced by the Hector Mine event has likely occurred within the top 15 km of the crust.

Geometric parameters of subfaults for the best-fitting model are given in Table 2. The only notable departures from the initial model in the result of nonlinear optimization are changes in the fault dip angle from vertical to 75° to 85° E in the southern section of the rupture. The slip distribution for our preferred solutions using both the half-space and the layered elastic space models are shown in Figures 7 and 8. Figure 9d–f shows the predicted InSAR data for the best-fitting layered-space model; Figure 9g–i shows the residuals between the observed data and the best-fitting model. The corresponding predictions and residuals of a half-space model are very similar to those shown in Figure 9. The main effect of the rigidity stratification is to increase the inferred slip at depth by about 20% to 30% (Fig. 11), similar to predictions of 2D solutions for a layered elastic half-space (Savage, 1998). The larger magnitude of slip inferred at depth in the layered elastic model provides a larger stress available to drive viscoelastic postseismic models.

While our forward models are simplified (in particular, they do not account for possible lateral variations in elastic properties of the upper crustal rocks, effects of topography, etc.), the rms of the LOS residuals is a few centimeters, or a few percent of the modeled signal. Some fraction of the far-field model misfit is likely of atmospheric origin (conspicuously so, in the ascending LOS residual); the near-fault misfit may indicate inadequacies of the elastic dislocation model near the earthquake rupture. The rms AZO residuals are on the order of a few tens of centimeters, also similar to the estimated error. We have compared inversion results using different weights for the AZO data versus the LOS phase data. We find that the AZO data do not add significant constraints to the model, since we have phase data from both ascending and descending orbits. The sufficiency of using only phase

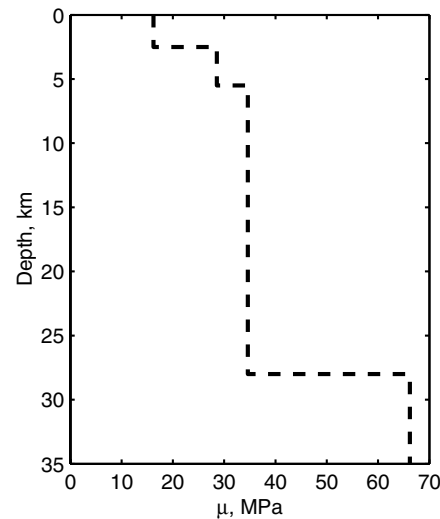


Figure 10. Rigidity structure derived from Jones and Helmberger (1998).

Table 2
Inferred Fault Geometry

Segment	1	2	3	4	5
x_0 , km	-9.20	-4.26	-1.47	2.91	9.51
y_0 , km	11.45	2.16	2.75	-13.93	-23.00
Length, km	7.91	13.94	26.00	9.42	17.00
Strike, deg	165	142	167	158	137
Dip, deg	90	90	90	105	100

All faults have width (down-dip dimension) of 20 km, with top edges intersecting the surface. Coordinates x_0 , y_0 correspond to centers of the top edges of the faults. Origin is at the earthquake epicenter (116.270° W, 34.595° N). Faults dipping to the east have dip angles in excess of 90° .

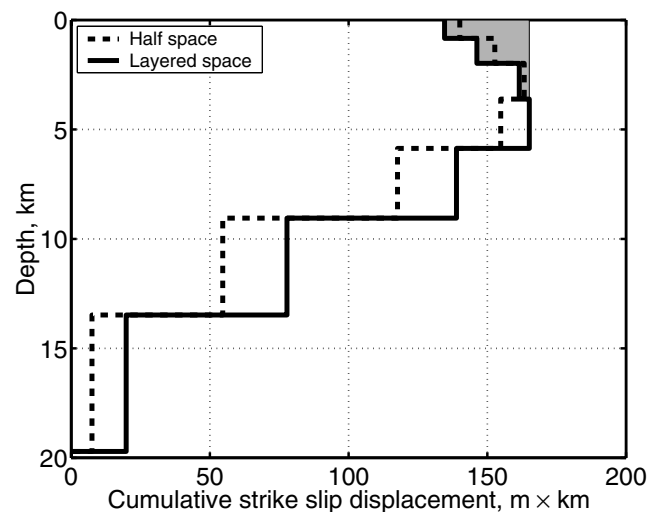


Figure 11. Depth profile of slip integrated along strike as predicted from both the half-space and layered-space models. The shaded gray area indicates the amount of potential slip deficit and would correspond to a M_w 6.1 earthquake.

data stems from the larger noise level in the AZO data and from the fact that physical models are not free to do arbitrary things in three different directions. The results presented here use only the ASC and DSC phase data, and the AZO residuals are calculated as a check. In essence, it appears that two distinct components of the displacement field, with at least one being sensitive to the vertical component, are sufficient to constrain these simple models. If we had only one interferogram available, then the AZO data would provide a more useful constraint. In addition to comparing against the AZO data, we validate our preferred solution by comparing model predictions against the campaign GPS data and find good agreement (Fig. 12).

Discussion and Conclusions

The surface displacement distribution along the fault trace predicted by our model has a roughly triangular shape with a peak amplitude of about 5 to 6 m, in good agreement with the field mapping data (Scientists of the USGS *et al.*, 2000; Treiman *et al.*, 2002). Using a reference shear modulus (33 GPa), we find geodetic moments of 6.7×10^{19} and 7.2×10^{19} N m for the homogeneous and layered half-space models, respectively. These values generally agree with the seismic moment estimates of 4 to 6×10^{19} N m (e.g., Harvard centroid moment tensor [CMT] solution; Dreger and Kaverina, 2000). The inferred geodetic moment is expected to be somewhat larger than the seismic moment due to postseismic afterslip during 1 month following the earthquake (Jacobs *et al.*, 2002). That most of the strike-slip motion due to the earthquake occurs in the northern section of the fault is corroborated by the 3D surface displacement fields derived from the InSAR data (Fialko *et al.*, 2001). This observation does not agree with the seismic inversions of Dreger and Kaverina (2000), who conclude that most of the coseismic slip occurred on the southern strand of a fault (although they point out that adding more complexity to their time-dependent simulations may reconcile the results of seismic inversions with the InSAR data).

Our model predicts a fault dip changing from near vertical in the northern section of the fault to 75° – 80° E toward the southern tip of the fault. Our estimates of fault dip are

generally consistent with the aftershock distribution as shown by the cross sections in Figure 13, and positions of our major fault segments inferred from our inversion (Table 2). Aftershock positions from Hauksson *et al.* (2002) are determined from a relocation of catalog events using a 3D velocity model of the area.

On average, the maximum slip (strike-slip component) occurs at a depth of 3 to 6 km in the layered-space model, as is evident if we consider the depth profile of slip integrated along strike (Fig. 11). We do not convert this integrated slip to average slip (i.e., dividing by a total fault length), since which length to use is not obvious. The area to the left of the slip profiles in Figure 11 corresponds to the total potency, which can in turn be converted to moment using the appropriate rigidity. Of particular interest is the apparent deficit of slip (the shaded area in Fig. 11) at shallow depths. A significant number of similar earthquakes would result in the surface falling behind the deeper crust. This apparent deficit is equivalent to a M_w 6.1 earthquake. There are several possible ways to account for this apparent deficit:

1. The slip deficit is offset by past and future large events. This hypothesis implies that we should see events whose integrated along-strike, strike-slip depth profile has a maximum at the surface. Such a slip profile has not been seen for any recent strike-slip earthquake for which high-quality spatially complete data exist (e.g., 1992 Landers, California, and 1999 Izmit, Turkey).
2. The slip deficit is filled by smaller events. For just the region of the Hector Mine earthquake, this hypothesis implies a M_w 6.1 event or a few tens of M_w 5 events limited to the top 3 km. Such events have yet to be seen in the eastern Mojave Desert.
3. The slip deficit is an artifact of the model. We consider the following three possibilities:
 - a. The model is nonunique, and the deficit is not required. This does not seem likely, because we have introduced a gradient minimization constraint in the inversion; therefore, the data appear to require the model to produce a vertical gradient in slip.
 - b. The elastic model requires greater spatial variation, potentially including more extreme vertical gradients

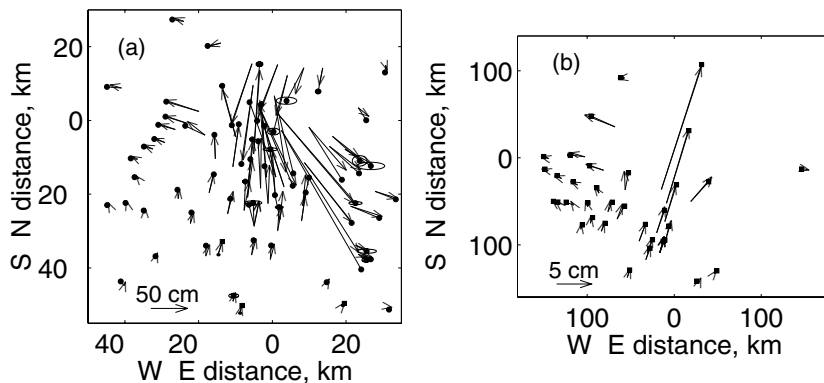


Figure 12. Horizontal displacements predicted by the best-fitting slip model (arrows), and the observed campaign-mode (solid circles) and continuous (solid squares) GPS data. Ellipses denote the reported GPS errors (too small to be visible for most vectors). Origin relative to the Hector Mine epicenter.

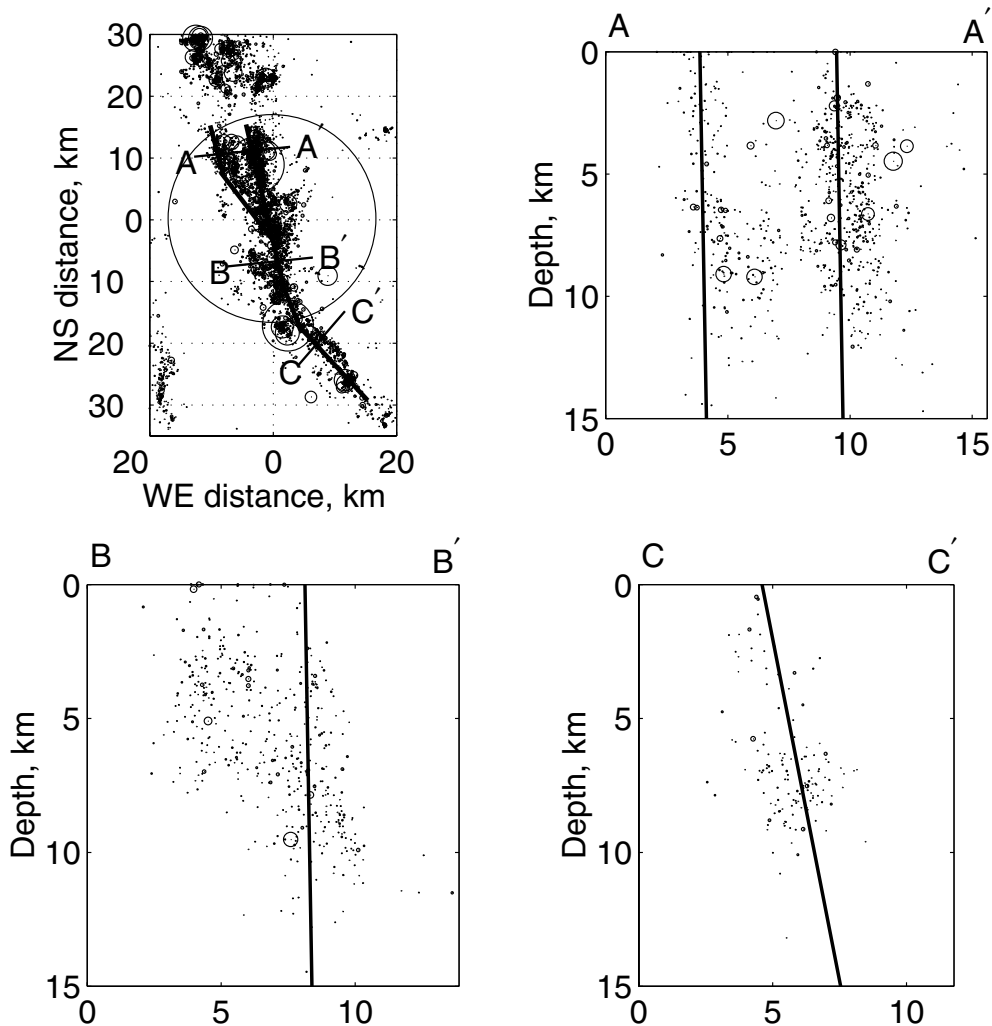


Figure 13. Map and cross-section views of the Hector Mine aftershock distribution (circles) from Hauksson *et al.* (2002). Thick solid lines denote fault model that yields the best fit to the geodetic data.

or horizontal variations, or both. At present, we cannot completely exclude this hypothesis.

- c. The assumption of purely elastic deformation is incorrect and some inelastic processes off the main fault, which are unaccounted for by our model, appreciably affect the observed deformation.

We expand here on this last hypothesis. We consider a simple calculation comparing the predicted surface displacement from long strike-slip faults with and without a near-surface slip deficit (Fig. 14). Both models have slip extending to the same depth and nearly identical total moments. The differences between the surface displacements predicted by these two models are concentrated within a distance from the fault corresponding to the depth of significant differences in the fault-slip distribution (here, about 10 km). The most significant difference in the synthetic displacement profiles is the curvature of the displacement field at distances close to the fault (within about 3 km). These calculations suggest that, if inelastic processes are present and if these processes

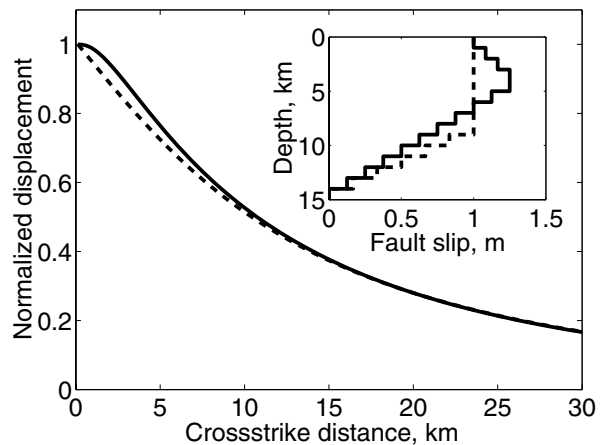


Figure 14. Cross-strike profiles of predicted along-strike component of surface displacement for two fault-slip scenarios. Both models assume a 1000-km-long vertical fault in an elastic half-space, with the displacement profile taken at the fault midpoint.

generate displacement profiles with inflection points in the displacement profiles, then the near-field displacement data may be misinterpreted by purely elastic models, in which case the slip excess (relative to the surface) that we infer at depth is an artifact. At the present time, the role of inelastic processes is only a hypothesis and requires further modeling and detailed high-resolution analyses of other recent strike-slip earthquakes for which spatially dense geodetic data are available.

Acknowledgments

Original InSAR data are copyright by the European Space Agency and distributed by Eurimage, Italy, via the WInSAR data consortium. We are grateful to D. Agnew and E. Hauksson for providing GPS observations and relocated seismicity data before publication, and to K. Hudnut, S. Owen, and M. Rymer for their efficient reviews. We acknowledge the Southern California Integrated GPS Network and its sponsors, the W.M. Keck Foundation, NASA, NSF, USGS, and SCEC for providing data used in this study. Processed radar interferograms used in this study are available from the authors. Contribution Number 8857 of the Division of Geological and Planetary Sciences, Seismological Laboratory, California Institute of Technology. This research was partially supported by the Southern California Earthquake Center. SCEC is funded by NSF Cooperative Agreement Number EAR-8920136 and USGS Cooperative Agreements Number 14-08-0001-A0899 and 1434-HQ-97AG01718. The SCEC contribution number for this paper is 636.

References

- Agnew, D. C., S. Owen, Z.-K. Shen, G. Anderson, J. Svarc, H. Johnson, K. E. Austin, and R. Reilinger (2002). Coseismic displacements from the Hector Mine, California, earthquake: results from survey-mode GPS measurements, *Bull. Seism. Soc. Am.* **92**, 1355–1364 (this issue).
- Dokka, R. K., and Travis, C. J. (1990). Role of the eastern California shear zone in accommodating Pacific-North American plate motion, *Geophys. Res. Lett.* **17**, 1323–1327.
- Dreger, D., and A. Kaverina (2000). Seismic remote sensing of the earthquake source process and near-source strong shaking: a case study of the October 16, 1999 Hector Mine earthquake, *Geophys. Res. Lett.* **27**, 1941–1944.
- Emardson, T. R., M. Simons, and F. H. Webb (2002). Neutral atmospheric delay in interferometric synthetic aperture radar applications: statistical description and mitigation, *J. Geophys. Res.* (submitted for publication).
- Fialko, Y., M. Simons, and D. C. Agnew (2001). The complete (3-D) surface displacement field in the epicentral area of the 1999 M_w 7.1 Hector Mine earthquake, California, from space geodetic observations, *Geophys. Res. Lett.* **28**, 3063–3066.
- Freed, A. M., and J. Lin (2001). Delayed triggering of the 1999 Hector Mine earthquake by viscoelastic stress transfer, *Nature* **411**, 180–183.
- Goldstein, R. M., and C. L. Werner (1998). Radar interferogram filtering for geophysical applications, *Geophys. Res. Lett.* **25**, 4035–4038.
- Hauksson, E., L. M. Jones, and K. Hutton (2002). The 1999 M_w 7.1 Hector Mine, California, earthquake sequence: complex conjugate strike-slip faulting, *Bull. Seism. Soc. Am.* **92**, 1154–1170 (this issue).
- Hudnut, K. W., N. E. King, J. E. Galetzka, K. F. Stark, J. A. Behr, A. Aspiotes, S. van Wyk, R. Moffitt, S. Dockter, and F. Wyatt (2002). Continuous GPS observations of postseismic deformation following the 16 October 1999 Hector Mine, California, earthquake (M_w 7.1), *Bull. Seism. Soc. Am.* **92**, 1403–1422 (this issue).
- Hurst, K., D. Argus, A. Donnellan, M. Heflin, D. Jefferson, G. Lyzenga, J. Parker, M. Smith, F. Webb, and J. Zumberge (2000). The coseismic geodetic signature of the 1999 Hector Mine, earthquake, *Geophys. Res. Lett.* **27**, 2733–2736.
- Jacobs, A., D. Sandwell, Y. Fialko, and L. Sichoix (2002). Hector Mine, California earthquake: near-field postseismic deformation from ERS interferometry, *Bull. Seism. Soc. Am.* **92**, 1433–1442 (this issue).
- Jennings, C. W. (Compiler) (1994). Fault activity map of California and adjacent areas, geologic data map series no. 6, scale 1:750,000, Tech. Rept., California Department of Conservation, Div. of Mines and Geology, Sacramento.
- Jones, L. E., and D. V. Helmberger (1998). Earthquake source parameters and fault kinematics of the eastern California shear zone, *Bull. Seism. Soc. Am.* **88**, 1337–1352.
- Masterlark, T. L., and H. F. Wang. (2002). Transient stress-coupling between the 1992 Landers and 1999 Hector Mine, California, earthquakes, *Bull. Seism. Soc. Am.* **92**, 1470–1486 (this issue).
- Owen, S., G. Anderson, D. C. Agnew, H. Johnson, K. Hurst, R. Reilinger, Z.-K. Shen, J. Svarc, and T. Baker (2002). Early postseismic deformation from the 16 October 1999 M_w 7.1 Hector Mine, California, earthquake as measured by survey-mode GPS, *Bull. Seism. Soc. Am.* **92**, 1423–1432 (this issue).
- Parsons, T., and D. Dreger (2000). Static-stress impact of the 1992 Landers earthquake sequence on nucleation and slip at the site of the 1999 M 7.1 Hector mine earthquake, southern California, *Geophys. Res. Lett.* **27**, 1949–1952.
- Pollitz, F. F., and I. S. Sacks (2002). Stress triggering of the 1999 Hector Mine, California, earthquake by transient deformation following the 1992 Landers earthquake, *Bull. Seism. Soc. Am.* **92**, 1487–1496 (this issue).
- Pollitz, F. F., C. Wicks, and W. Thatcher (2001). Mantle flow beneath a continental strike-slip fault: postseismic deformation after the 1999 Hector Mine earthquake, *Science* **293**, 1814–1818.
- Sandwell, D., L. Sichoix, D. Agnew, Y. Bock, and J.-B. Minster (2000). Near real-time radar interferometry of the M_w 7.1 Hector Mine earthquake, *Geophys. Res. Lett.* **27**, 3101–3104.
- Sauber, J., W. Thatcher, and S. C. Solomon (1986). Geodetic measurements of deformation in the central Mojave Desert, California, *J. Geophys. Res.* **91**, 2683–2693.
- Savage, J. C. (1998). Displacement field for an edge dislocation in a layered half space, *J. Geophys. Res.* **103**, 2439–2446.
- Scientists of the U.S. Geological Survey, Southern California Earthquake Center, and the California Division of Mines and Geology (2000). Preliminary report on the 16 October 1999 M 7.1 Hector Mine, California, earthquake, *Seism. Res. Lett.* **71**, 11–23.
- Sieh, K., L. M. Jones, E. Hauksson, K. Hudnut, D. Eberhart-Phillips, T. Heaton, S. Hough, K. Hutton, H. Kanamori, A. Lilje, S. Lindvall, S. McGill, J. Mori, C. Rubin, J. Spotila, J. Stock, H. Thio, J. Treiman, B. Wernicke, and J. Zachariasen (1993). Near-field investigations of the Landers earthquake sequence, *Science* **260**, 171–176.
- Treiman, J. A., K. J. Kendrick, W. A. Bryant, T. K. Rockwell, and S. F. McGill (2002). Primary surface rupture associated with the M_w 7.1 16 October 1999 Hector Mine earthquake, San Bernardino County, California, *Bull. Seism. Soc. Am.* **92**, 1171–1191 (this issue).
- Zebker, H. A., and J. Villasenor (1992). Decorrelation in interferometric radar echoes, *IEEE Trans. Geosci. Rem. Sens.* **30**, 950–959.

Seismological Laboratory
California Institute of Technology
Mail Code 252-21
1200 E. California Blvd.
Pasadena, California 91125
simons@caltech.edu
(M.S., Y.F.)

École et Observatoire des Sciences de la Terre
Université Louis Pasteur-CNRS
5, rue René Descartes
67084 Strasbourg cedex
France
(L.R.)